ADAPTIVE FUZZY VIBRATION CONTROL OF SMART STRUCTURE WITH VFIFE MODELING

R. Xu * **D.-X. Li** **J.-P. Jiang** **W. Liu**

National University of Defense Technology
Changsha, PR China

ABSTRACT

The vibration control of smart structure is considered in this paper. Membrane SAR antenna structure with piezoelectric sensors and actuators is taken as an example. The dynamic model is build up based on vector form intrinsic finite element (VFIFE) method. The four nodes membrane element, sensor element and actuator element for VFIFE are presented. By decentralized control stratagem, the bending and torsional vibrations of the membrane SAR antenna can be decoupled on measurement and driving control. The fuzzy control and adaptive fuzzy control are applied to suppress the bending and torsional vibrations of the membrane SAR structure. In the numerical experiment section, form finding is first carried out, then vibration control simulations are studied. The results demonstrate that adaptive fuzzy control algorithm can suppress the vibrations more effectively than the fuzzy control algorithm.

Keywords: Vibration control, Fuzzy control, Vector form finite element, Smart structure.

1. INTRODUCTION

Synthetic Aperture Radar (SAR) satellites are widely used for earth remote sensing applications. In order to reach a high resolution, fairly large and long antennas are required, especially for lower frequency SARs such as L-Band typically 12m × 3m required. In traditional SAR antenna structure design concept, to maintain an acceptable electrical flatness across the large antenna, very massive antenna support structures, weighing several hundred kilograms or more, have been used to date. For even larger SAR antennas (10m to 100m dimensions), it would be prohibitive if technology relies on this design concept. In order to reduce mass, launch-vehicle storage volume and overall cost, membrane based SAR antenna design concept was proposed. For typical membrane SAR antenna, the active components are mounted on the thin membrane, and the membrane is tensioned by the coil-able support frame. With this new concept, the mass of the future SAR is expected to be less than 100kg [1]. However, to achieve good electrical performance, one of the challenges is keeping the flatness of the membrane, typically it should be in the order of 1/30 of the free space radar wavelength [2]. For L-Band SAR antenna, the flatness of the membrane should keep less than 5 to 10 mm.

In the space environment, the attitude maneuvering of the antenna, the heat flux of the sun, the gravity gradient torque and the other disturbance can induce structural vibrations and deformations that are detrimental to radar performance. As the membrane SAR antenna structures have extensive flexibility and low damping ratio, the induced vibrations will be large amplitude, low frequency and hard to attenuation. It will severely degrade the performance of the membrane SAR antenna. One efficient way to solve this problem is to take active vibration control by implemented smart structure.

Smart structure is the integration of several elements: sensor, actuators, signal processors, and power sources. It senses and reacts to the environment in a predictable way in order to compensation all the undesirable external perturbations [3]. Smart structures, especially piezoelectric smart structures, have been used extensively for active vibration control of space structure for years. Li *et al*. investigated vibration control of space truss structure [4] and smart solar array structure [5,6] by using piezoelectric stacks and piezoelectric patches, respectively. Qiu *et al*. used piezoelectric sensors and actuators to suppress the vibration of a flexible plate [7]. Sales introduced passive vibration control of flexible spacecraft using shunted piezoelectric transducers [8]. Li *et al*. studied vibration control of a tri-prism truss structure using active piezoelectric struts [9]. However, studies on membrane structure vibration control have been rarely carried out.

In this paper, the controlled object, the membrane SAR antenna, is rather complicated. It is a beam-cable-membrane composite structure. Because of the large size and flexibility, this makes the structure have some special dynamic properties, such as, very low stiffness, low damping ratios, high dimensional order, and low modal frequencies. Due to the tension force of the membrane and large amplitude of vibration, the

* Corresponding author (xurui@nudt.edu.cn)

DOI : 10.1017/jmech.2015.45
Copyright © 2015 The Society of Theoretical and Applied Mechanics, R.O.C.
https://doi.org/10.1017/jmech.2015.45 Published online by Cambridge University Press

influences of prestress and geometry nonlinearity should be considered too. Hence, the dynamic model is hard to build through traditional finite element method (FEM). A new method, named vector form intrinsic finite element method (VFIFE), is introduced to solve this problem. VFIFE was developed by Ting *et al*. [10,11] and Shih *et al*. [12] in 2004. The fundamental idea of VFIFE method is to discretize the structural system into particles based on Newton's law. This method is very efficient in processing large deformation problem, since it does not need structural stiffness matrix and iterative method. Wang *et al*. used the VFIFE method to analyze nonlinear dynamic behaviors of 3D reticulated structure [13] and building system [14]. Wu *et al*. adopted the VFIFE method to do large deflection analysis for flexible frame structures [15,16] and 3D membrane structures [17,18]. Lien *et al*. applied the VFIFE method to investigate the nonlinear behavior of steel structures exposed to fire [19,20] and the inelastic large deflection behavior for steel frames with semi-rigid joints [21]. Recently, Wu implemented the VFIFE method to perform dynamic nonlinear analysis of shell structures [22].

This study addresses the vibration control problem of the membrane SAR antenna. Compared with some previous investigations of this area, the major originalities contribution are as follows:

1. A kind of four nodes membrane element for VFIFE is proposed.
2. The sensor and actuator models for VFIFE are proposed.
3. The decentralized adaptive fuzzy control stratagem is given.
4. Numeric experiments are conducted to validate the form finding result of the membrane and the advantage of the designed control methods.

The rest of this article is organized as follows: First, the description of the membrane SAR antenna structure and the fundamental conception and elements of VFIFE are presented. The structure is modeled as beam elements and four nodes membrane elements. Secondly, the modeling of the sensor and actuator for VFIFE are proposed. Then, the bending and torsional vibrations of the membrane SAR antenna are decoupled as two control channels by using decentralized control stratagem. Adaptive fuzzy controllers are designed for each channel. Finally, numerical experiments are conducted. Form finding is first carried out, then vibration control simulations are studied.

2. MODELING FOR THE MEMBRANE SAR ANTENNA

2.1 Description of the Membrane SAR Antenna

The membrane SAR antenna considered in this paper is shown in Fig. 1. It is fix connected to the satellite body by support trusses. The membrane SAR antenna is typically composed of three components, a support

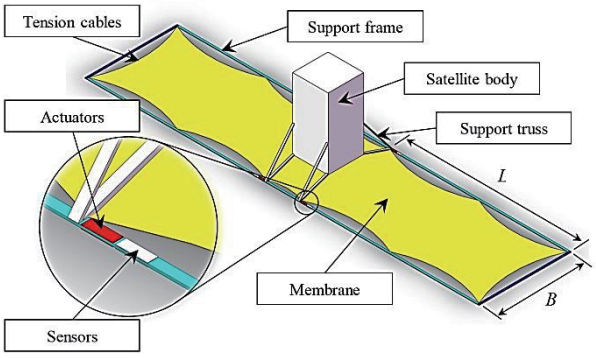


Fig. 1 The structure of the membrane SAR antenna.

frame, a membrane and tension cables. The function of the support frame is produce a constant tension for the membrane. Moreover, the tension cables makes the stress of the membrane well-distributed. The length and width of the antenna are L and B, respectively. As the support trusses and the satellite body is more rigid and weighted than the membrane SAR antenna, hence they can be simplified as rigid body in this paper.

In order to control the vibration of the antenna, piezoelectric sensors and actuators are implemented in this paper. As shown in the figure, there are eight piezoelectric patches symmetrically bonded on both surfaces of the beam. Four of them are used as strain sensors, while the other four are used as strain actuators. In order to produce a pure bending moment for vibration suppression purpose, opposite directions electric field are applied to each pair of piezoelectric patches.

2.2 VFIFE Modeling of the Smart Beam

2.2.1 Fundamental Conceptions

The three fundamental conceptions of VFIFE are point values, path element and fictitious reverse motion. The conception of point values means the structure is described by a group of mass points.

The fundamental idea of VFIFE is discrete the structure into finite mass points and deformable elements without mass. All the mass points are connected by the elements and are in equilibrium. The structural geometry is defined by the trajectories of the connected mass points. Assume the motion of each mass point follows Newton's law, the equation of motion for node i at time t can be written as

$$\mathbf{M}_i\ddot{\mathbf{x}}_i(t)+\alpha\mathbf{M}_i\dot{\mathbf{x}}_i(t)=\mathbf{F}_i^{ext}(t)-\mathbf{F}_i^{int}(t) \tag{1}$$

$$\mathbf{I}_i\ddot{\boldsymbol{\theta}}_i(t)+\alpha\mathbf{I}_i\dot{\boldsymbol{\theta}}_i(t)=\mathbf{M}_i^{ext}(t)-\mathbf{M}_i^{int}(t) \tag{2}$$

where α is the damping coefficient, $\mathbf{M}_i = \mathrm{diag}(m_i, m_i, m_i)$ is the diagonal mass matrix of the node i, m_i is the mass of the node, $\mathbf{I}_i$ is the moment of inertia matrix of the node

$$\mathbf{I}_i=\begin{bmatrix} I_{xx} & I_{xy} & I_{xz} \\ I_{yx} & I_{yy} & I_{yz} \\ I_{zx} & I_{zy} & I_{zz} \end{bmatrix}_i \tag{3}$$

https://doi.org/10.1017/jmech.2015.45 Published online by Cambridge University Press

$\mathbf{x}_i(t)$ and $\boldsymbol{\theta}_i(t)$ are the translation and rotation displacement vector, respectively; α is the damping coefficient; $\mathbf{F}_i^{ext}(t)$ and $\mathbf{M}_i^{ext}(t)$ are the vector of applied forces and moments or equivalent forces and moments acting on the node, $\mathbf{F}_i^{int}(t)$ and $\mathbf{M}_i^{int}(t)$ are the vector of total resistance forces and moments or internal resultant forces and moments by all the elements connecting with this node.

It is noted that the equation of translation can be individually solved. However, the equation of rotation are coupled, they should be solved simultaneously. It is much different from the traditional finite element method. Another difference is that the element internal forces in VFIFE are calculated by using the element pure deformations, which is obtained through subtracting rigid body translations and rotations from deformation increments. Due to this concept of fictitious reverse motion, VFIFE is capable of dealing with structure dynamic problems with large displacements, deformations and rigid body motions simultaneously.

2.2.2 Beam element

Figure 2 shows relative displacements between two deformed configurations of a beam element. The (1_a, 2_a) and (1_b, 2_b) stands for the beam element configuration at time t_a and time $t_b = t_a + \Delta t$, respectively. The translation and rotation displacement vector at time t_a and t_b are ($\mathbf{x}_{1a}$, $\mathbf{x}_{2a}$, $\mathbf{x}_{1b}$, $\mathbf{x}_{2b}$) and ($\boldsymbol{\theta}_{1a}$, $\boldsymbol{\theta}_{2a}$, $\boldsymbol{\theta}_{1b}$, $\boldsymbol{\theta}_{2b}$). Denote ($\mathbf{u}_1$, $\mathbf{u}_2$) and ($\boldsymbol{\beta}_1$, $\boldsymbol{\beta}_2$) as the incremental translation and rotation displacement, respectively, $\mathbf{u}_i = \mathbf{x}_{ib} - \mathbf{x}_{ia}$, $\boldsymbol{\beta}_i = \boldsymbol{\theta}_{ib} - \boldsymbol{\theta}_{ia}$, $i = 1, 2$. Assume the beam is a prismatic one, the primary axes of it at time t_a and t_b are $\mathbf{e}_{xa}$ and $\mathbf{e}_{xb}$, respectively. Assume the section of the beam is always perpendicular to its primary axis. The principle axes of the beam section at time t_a and t_b are $(\mathbf{e}_{ya}, \mathbf{e}_{za})$ and $(\mathbf{e}_{yb}, \mathbf{e}_{zb})$. In order to deduce the rigid body displacement, the following three steps should be done:

Step I: Translation. Translate (1_b, 2_b) to (1_t, 2_t) with a vector $-\mathbf{u}_1$, as shown in Fig. 2.

Step II: Rotation of the primary axis. Rotate (1_t, 2_t) to (1_{r1}, 2_{r1}) with angle $-\boldsymbol{\gamma}_1$, where $\boldsymbol{\gamma}_1 = \gamma_{ba}\mathbf{e}_{ba}$, $\gamma_{ba} = \sin^{-1}\left(|\mathbf{e}_{xa} \times \mathbf{e}_{xb}|\right)$, $\mathbf{e}_{ba} = \mathbf{e}_{xa} \times \mathbf{e}_{xb} / |\mathbf{e}_{xa} \times \mathbf{e}_{xb}|$, as shown in Fig. 2.

Step III: Rotation around the primary axis. Rotate (1_{r1}, 2_{r1}) to (1_{r2}, 2_{r2}) around its primary axis with an angle $-\boldsymbol{\gamma}_2$, where $\boldsymbol{\gamma}_2 = (\boldsymbol{\beta}_1 \cdot \mathbf{e}_{xa})\,\mathbf{e}_{xa}$.

The two rotation can be added together

$$\boldsymbol{\gamma} = \boldsymbol{\gamma}_1 + \boldsymbol{\gamma}_2 = \gamma \cdot \mathbf{e}_\gamma \tag{4}$$

where $\mathbf{e}_\gamma = \{l_\gamma \;\; m_\gamma \;\; n_\gamma\}^T$ is the rotation direction, the rotation matrix of the primary axis can be expressed as

$$\mathbf{R}^* = \mathbf{I} + \mathbf{R}_\gamma \tag{5}$$

where

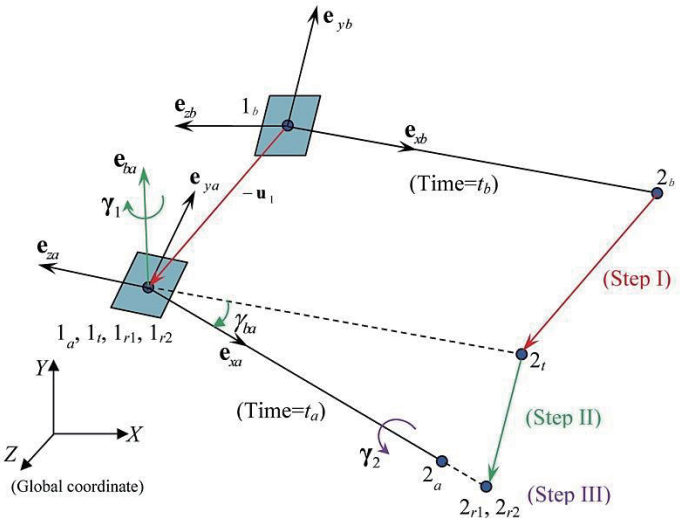


Fig. 2 Relative displacements between two deformed configurations of a beam element.

$$\mathbf{R}_\gamma = (1-\cos\gamma)\begin{bmatrix} 0 & -n_\gamma & m_\gamma \\ n_\gamma & 0 & -l_\gamma \\ -m_\gamma & l_\gamma & 0 \end{bmatrix}^2 + \sin\gamma \begin{bmatrix} 0 & -n_\gamma & m_\gamma \\ n_\gamma & 0 & -l_\gamma \\ -m_\gamma & l_\gamma & 0 \end{bmatrix} \tag{6}$$

After taken the fictitious reverse translation and rotations, the pure deformations of the beam element can be determined by six independent variables: The stretcher deformation $\Delta\delta$ and torsional deflection $\Delta\varphi_{2x}$ of the primary axis, the bend angles $\Delta\varphi_{1y}$, $\Delta\varphi_{1z}$, $\Delta\varphi_{2y}$ and $\Delta\varphi_{2z}$, as shown in Fig. 3.

As the stretcher deformation of the primary axis is $\Delta\delta = l_b - l_a$, l_a and l_b are the length of the element at time t_a and t_b, respectively, then the incremental axial internal force $\Delta\hat{f}_{1x}$ and $\Delta\hat{f}_{2x}$ are

$$\Delta\hat{f}_{1x} = -\Delta\hat{f}_{2x} = -\frac{EA_a}{l_a} \cdot \Delta\delta = -\frac{EA_a}{l_a} \cdot (l_b - l_a) \tag{7}$$

where E is the elastic modulus of the element, A_a is the section area of the element.

According to the pure torsion deformation $\Delta\varphi_{2x}$, the incremental internal moment on x axis $\Delta\hat{m}_{1x}$ and $\Delta\hat{m}_{2x}$ are

$$\Delta\hat{m}_{1x} = -\Delta\hat{m}_{2x} = -\frac{GJ_a}{l_a}\Delta\varphi_{2x} \tag{8}$$

where G is the shear modulus of the element, J_a is the moment of inertia of the element section.

According to the pure deformation $\Delta\varphi_{1z}$ and $\Delta\varphi_{2z}$, the incremental internal moment on z axis $\Delta\hat{m}_{1z}$ and $\Delta\hat{m}_{2z}$ are

$$\Delta\hat{m}_{1z} = \frac{EI_z}{l_a}(4\Delta\varphi_{1z} + 2\Delta\varphi_{2z}) \tag{9}$$

https://doi.org/10.1017/jmech.2015.45 Published online by Cambridge University Press

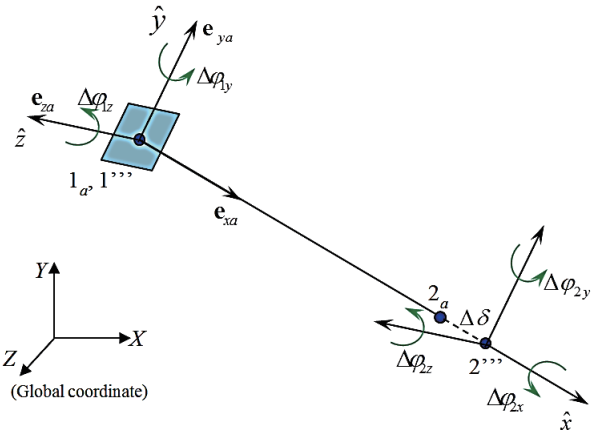


Fig. 3 Six pure deformation variables of the beam element.

$$\Delta\hat{m}_{2z} = \frac{EI_z}{l_a}(2\Delta\varphi_{1z} + 4\Delta\varphi_{2z}) \tag{10}$$

The incremental internal force on y axis $\Delta\hat{f}_{1y}$ and $\Delta\hat{f}_{2y}$ can be determined through the force and moment equilibrium conditions on the element

$$\Delta\hat{f}_{1y} = -\Delta\hat{f}_{2y} = \frac{1}{l_a}(\Delta\hat{m}_{1z} + \Delta\hat{m}_{2z}) = \frac{6EI_z}{l_a^2}(\Delta\varphi_{1z} + \Delta\varphi_{2z}) \tag{11}$$

Similarly,

$$\Delta\hat{m}_{1y} = \frac{EI_y}{l_a}(4\Delta\varphi_{1y} + 2\Delta\varphi_{2y}) \tag{12}$$

$$\Delta\hat{m}_{2y} = \frac{EI_y}{l_a}(2\Delta\varphi_{1y} + 4\Delta\varphi_{2y}) \tag{13}$$

$$\Delta\hat{f}_{1z} = -\Delta\hat{f}_{2z} = -\frac{1}{l_a}(\Delta\hat{m}_{1y} + \Delta\hat{m}_{2y}) = -\frac{6EI_y}{l_a^2}(\Delta\varphi_{1y} + \Delta\varphi_{2y}) \tag{14}$$

All the internal forces at those two nodes of a beam element in the deformation coordinate system can be expressed by a vector $\Delta\mathbf{f}_e$ as

$$\Delta\mathbf{f}_e = \{\Delta\hat{f}_{1x},\ \Delta\hat{f}_{1y},\ \Delta\hat{f}_{1z},\ \Delta\hat{m}_{1x},\ \Delta\hat{m}_{1y},\ \Delta\hat{m}_{1z},\ \Delta\hat{f}_{2x},\ \Delta\hat{f}_{2y},\ \Delta\hat{f}_{2z},\ \Delta\hat{m}_{2x},\ \Delta\hat{m}_{2y},\ \Delta\hat{m}_{2z}\} \tag{15}$$

2.2.3 Membrane element

In this paper, the membrane is modeled as 4-node quadrilateral elements. It is assumed that the winkling and warping induced internal forces could be neglected. Hence, the element stress can be considered as a state of plane stress. Figure 4 illustrates the motion of an element from time t_a to t_b, the geometry of the membrane element is defined by four nodes with numbers (1_a, 2_a, 3_a, 4_a) and (1_b, 2_b, 3_b, 4_b), respectively. The position vector and the normal vector of node I at time t_a are respectively denote as $\mathbf{x}_{Ia}$ and $\mathbf{n}_{Ia}$, $\mathbf{n}_{1a} = (\mathbf{x}_{2a} - \mathbf{x}_{1a}) \times (\mathbf{x}_{4a} - \mathbf{x}_{1a})$, $\mathbf{n}_{2a} = (\mathbf{x}_{3a} - \mathbf{x}_{2a}) \times (\mathbf{x}_{1a} - \mathbf{x}_{2a})$, $\mathbf{n}_{3a} = (\mathbf{x}_{4a} - \mathbf{x}_{3a}) \times (\mathbf{x}_{2a} - \mathbf{x}_{3a})$, $\mathbf{n}_{4a} = (\mathbf{x}_{1a} - \mathbf{x}_{4a}) \times (\mathbf{x}_{3a} - \mathbf{x}_{4a})$, similarly $\mathbf{x}_{Ib}$ and $\mathbf{n}_{Ib}$ for time t_b,.

For a four node quadrilateral membrane element, it is much more complicated to deduce the rigid boy displacement than beam elements. It is done through the following five steps:

Step I: Projection. As the element may be warped under load, hence the first step is project the warped shape onto plane. As shown in Fig. 4, define C_a with position $\mathbf{x}_{Ca} = \frac{1}{4}\sum_{i=1}^{4}\mathbf{x}_{ia}$ as the center of (1_a, 2_a, 3_a, 4_a). Define an average normal vector $\mathbf{n}_{pa} = \frac{1}{4}\sum_{i=1}^{4}\mathbf{n}_{ia}$. Then project ($1_a$, 2_a, 3_a, 4_a) onto the plane determined by (C_a, $\mathbf{n}_{pa}$) evolved to (1_{pa}, 2_{pa}, 3_{pa}, 4_{pa}). Similarly, we can project (1_b, 2_b, 3_b, 4_b) onto the plane determined by (C_b, $\mathbf{n}_{pb}$) evolved to (1_{pb}, 2_{pb}, 3_{pb}, 4_{pb}).

Step II: First translation. Translate (1_{pb}, 2_{pb}, 3_{pb}, 4_{pb}) with a vector $\mathbf{u}_{t1} = \mathbf{x}_{Ca} - \mathbf{x}_{Cb}$ evolved to (1_{t1}, 2_{t1}, 3_{t1}, 4_{t1}). After imposing the reverse translation the element center C_a and C_b merge together, as shown Fig. 5.

Step III: Out of plane Rotation. Rotate (1_{t1}, 2_{t1}, 3_{t1}, 4_{t1}) to (1_{r1}, 2_{r1}, 3_{r1}, 4_{r1}) with an angle θ_{r1}, shown in Fig. 5. The rotate center is C_a, the rotate direction is $\mathbf{n}_{r1} = \frac{\mathbf{n}_{pa} \times \mathbf{n}_{t1}}{|\mathbf{n}_{pa} \times \mathbf{n}_{t1}|} = \{l_{r1}\ \ m_{r1}\ \ n_{r1}\}^T$, the rotate angle is $\theta_{r1} = \arccos\left(\frac{\mathbf{n}_{pa} \cdot \mathbf{n}_{t1}}{|\mathbf{n}_{pa}||\mathbf{n}_{t1}|}\right)$. The rotation matrix of the out of plane is $\mathbf{R}_{r1}^* = \mathbf{R}_{r1} + \mathbf{I}$, where $\mathbf{R}_{r1}$ is

$$\mathbf{R}_{r1} = (1 - \cos(-\theta_{r1}))\begin{bmatrix} 0 & -n_{r1} & m_{r1} \\ n_{r1} & 0 & -l_{r1} \\ -m_{r1} & l_{r1} & 0 \end{bmatrix}^2 + \sin(-\theta_{r1})\begin{bmatrix} 0 & -n_{r1} & m_{r1} \\ n_{r1} & 0 & -l_{r1} \\ -m_{r1} & l_{r1} & 0 \end{bmatrix} \tag{16}$$

Step IV: In plane Rotation. Rotate (1_{r1}, 2_{r1}, 3_{r1}, 4_{r1}) to (1_{r2}, 2_{r2}, 3_{r2}, 4_{r2}) with an angle θ_{r2}. The rotate center is C_a, the rotate axis vector is $\mathbf{n}_{pa} = \{l_{r2}\ \ m_{r2}\ \ n_{r2}\}^T$, the in plane rotate angle is $\theta_{r2} = \frac{1}{4}\sum_{i=1}^{4}\Delta\theta_i$, where $|\Delta\theta_i| = \arccos(\mathbf{e}_{ir1} \cdot \mathbf{e}_{ipa})$, ($i = 1, 2, 3, 4$), $|\Delta\theta_i| \in [0, \pi]$ and $\mathbf{e}_{ir1} = \frac{\mathbf{x}_{ir1} - \mathbf{x}_{Ca}}{|\mathbf{x}_{ir1} - \mathbf{x}_{Ca}|}$, $\mathbf{e}_{ipa} = \frac{\mathbf{x}_{ipa} - \mathbf{x}_{Ca}}{|\mathbf{x}_{ipa} - \mathbf{x}_{Ca}|}$, shown in Fig. Fig. 6. The rotation matrix of the in plane is $\mathbf{R}_{r2}^* = \mathbf{R}_{r2} + \mathbf{I}$, where $\mathbf{R}_{r2}$ is

https://doi.org/10.1017/jmech.2015.45 Published online by Cambridge University Press

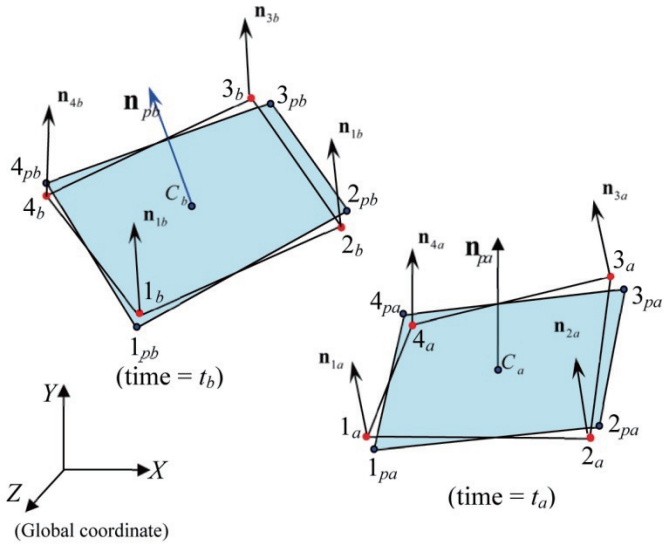


Fig. 4 Projection of membrane element.

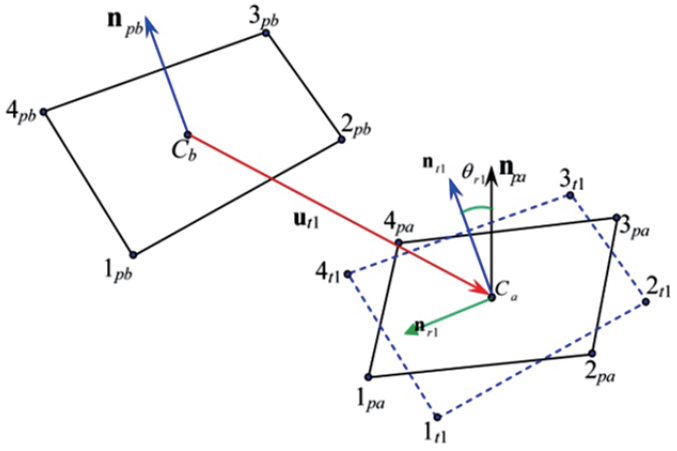


Fig. 5 First translation and out of plane rotation of membrane element.

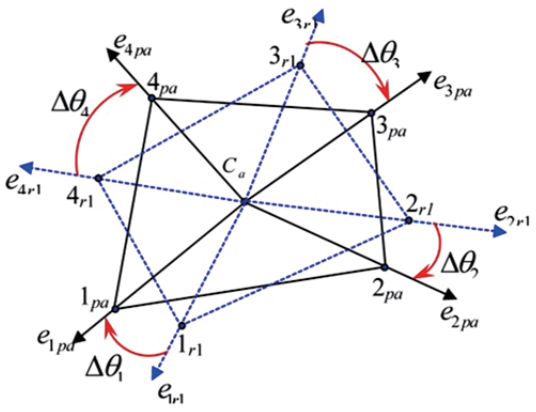


Fig. 6 In plane rotation of membrane element.

$$\mathbf{R}_{r2} = (1-\cos(-\theta_{r2}))\begin{bmatrix} 0 & -n_{r2} & m_{r2} \\ n_{r2} & 0 & -l_{r2} \\ -m_{r2} & l_{r2} & 0 \end{bmatrix}^2 + \sin(-\theta_{r2})\begin{bmatrix} 0 & -n_{r2} & m_{r2} \\ n_{r2} & 0 & -l_{r2} \\ -m_{r2} & l_{r2} & 0 \end{bmatrix} \tag{17}$$

Step V: Second translation. Translate (1_{r2}, 2_{r2}, 3_{r2}, 4_{r2}) to (1_{t2}, 2_{t2}, 3_{t2}, 4_{t2}) with a vector $\mathbf{u}_{t2} = \mathbf{x}_{1r2} - \mathbf{x}_{1pa}$, shown in Fig. 7.

After the above five step operation, the rigid body translation and rotation can be eliminated appropriately. The pure deformation vector of the four nodes can defined as $\Delta\boldsymbol{\eta}_1$, $\Delta\boldsymbol{\eta}_2$, $\Delta\boldsymbol{\eta}_3$ and $\Delta\boldsymbol{\eta}_4$. It can be noted that $\Delta\boldsymbol{\eta}_1 = 0$. As six rigid body modes must be eliminated, a deformation coordinate $o-\hat{x}\hat{y}\hat{z}$ should be defined, as shown in Fig. 7. The origin of the deformation coordinate is at node 1_{pa}. The $\hat{x}$ axis is parallel to the pure deformation vector $\Delta\boldsymbol{\eta}_2$. The $\hat{z}$ axis is parallel to the average normal vector $\mathbf{n}_{pa}$. The basis vectors of the deformation coordinate are defined as:

$$\begin{aligned} \hat{\mathbf{e}}_x &= \frac{\Delta\boldsymbol{\eta}_2}{|\Delta\boldsymbol{\eta}_2|} \\ \hat{\mathbf{e}}_y &= \frac{\mathbf{n}_{pa}\times\hat{\mathbf{e}}_x}{|\mathbf{n}_{pa}\times\hat{\mathbf{e}}_x|} \\ \hat{\mathbf{e}}_z &= \mathbf{n}_{pa} \end{aligned} \tag{18}$$

The pure deformation on the deformed coordinate can be written as $\hat{\mathbf{u}}_e = [0, 0, \hat{u}_2, 0, \hat{u}_3, \hat{v}_3, \hat{u}_4, \hat{v}_4]^T$. It can be noted that three DOFs are eliminated, denote $\hat{\mathbf{u}}_e^* = [\hat{u}_2, \hat{u}_3, \hat{v}_3, \hat{u}_4, \hat{v}_4]^T$. According to the virtual work formulation, the internal virtual work of the element is done by the internal nodal forces and in terms of the strain and stress, the virtual work is presented as [18]

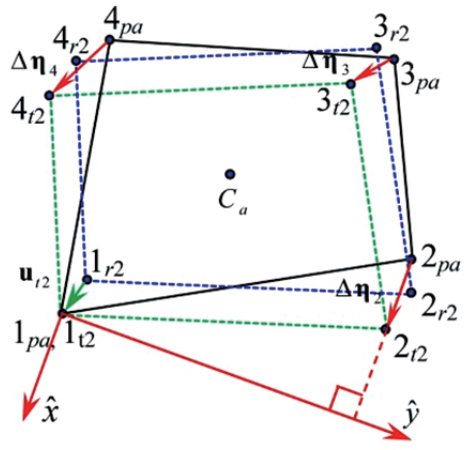


Fig. 7 Second translation of membrane element and definition of deformation coordinate.

https://doi.org/10.1017/jmech.2015.45 Published online by Cambridge University Press

$$\delta(U_e)=\int_{\hat{V}_e}\delta(\hat{\boldsymbol{\varepsilon}})^T\hat{\boldsymbol{\sigma}}\mathrm{d}\hat{V}+\int_{\hat{V}_e}\delta(\hat{\boldsymbol{\varepsilon}})^T\mathbf{D}\hat{\boldsymbol{\varepsilon}}\mathrm{d}\hat{V}$$
$$=\delta\hat{\mathbf{u}}_e^*\left[\int_{\hat{V}_e}(\mathbf{B}^*)^T\hat{\boldsymbol{\sigma}}\mathrm{d}\hat{V}+\left(\int_{\hat{V}_e}(\mathbf{B}^*)^T\mathbf{D}\mathbf{B}^*\mathrm{d}\hat{V}\right)\hat{\mathbf{u}}_e^*\right] \quad (19)$$

where $\hat{\boldsymbol{\varepsilon}}$ and $\hat{\boldsymbol{\sigma}}$ represent for the strain and stress, respectively, $\mathbf{B}$ and $\mathbf{D}$ are the strain matrix and elastic matrix, respectively. Then the internal force vector $\mathbf{f}_e^*$ is

$$\mathbf{f}_e^*=\{\hat{f}_{2x},\hat{f}_{3x},\hat{f}_{3y},\hat{f}_{4x},\hat{f}_{4y}\}$$
$$=\int_{\hat{V}_e}(\mathbf{B}^*)^T\hat{\boldsymbol{\sigma}}\mathrm{d}\hat{V}+\left(\int_{\hat{V}_e}(\mathbf{B}^*)^T\mathbf{D}\mathbf{B}^*\mathrm{d}\hat{V}\right)\hat{\mathbf{u}}_e^* \quad (20)$$

The remaining three components ($\hat{f}_{1x}$, $\hat{f}_{1y}$, $\hat{f}_{2y}$) can be determined through the force and moment equilibrium conditions on the element.

$$\sum F_{\hat{x}}=0 \quad \hat{f}_{1x}=-(\hat{f}_{2x}+\hat{f}_{3x}+\hat{f}_{4x}) \quad (21)$$

$$\sum M_{\hat{z}}=0 \quad \hat{f}_{2y}$$
$$=(\hat{f}_{2x}\hat{y}_2-\hat{f}_{3y}\hat{x}_3+\hat{f}_{3x}\hat{y}_3-\hat{f}_{4y}\hat{x}_4+\hat{f}_{4x}\hat{y}_4)/\hat{x}_2 \quad (22)$$

$$\sum F_{\hat{y}}=0 \quad \hat{f}_{1\hat{y}}=-(\hat{f}_{2\hat{y}}+\hat{f}_{3\hat{y}}+\hat{f}_{4\hat{y}}) \quad (23)$$

where ($\hat{x}_i$, $\hat{y}_i$) are the coordinate of the ith node in deformation coordinate.

3. MODELING OF SENSOR AND ACTUATOR IN VFIFE ELEMENT

The schematic of piezoelectric sensor and actuator is shown in Fig. 8. As shown in this figure, the polling direction P of the sensor and actuator are parallel to its thickness direction, the electrodes are on the upper and lower surfaces of the sensor and actuator. The length, width and thickness of the actuators are l_a, b and h_a, respectively. And the length, width and thickness of the sensors are l_s, b and h_s, respectively.

It is well known that in piezoelectric materials the electric field and the deformation influence each other. It have direct and inverse piezoelectric effects and can be used as both sensors and actuators. Due to the assumption of small strains and weak electric field, the coupling effects between mechanical and electrical properties can be described by the following linear constitutive relations:

$$\begin{cases}\boldsymbol{\sigma}=\mathbf{c}\boldsymbol{\varepsilon}-\mathbf{e}^T\mathbf{E}\\ \mathbf{D}=\mathbf{e}\boldsymbol{\varepsilon}+\boldsymbol{\chi}\mathbf{E}\end{cases} \quad (24)$$

where $\boldsymbol{\sigma}$, $\boldsymbol{\varepsilon}$, $\mathbf{D}$ and $\mathbf{E}$ are the stress tensor, strain tensor, electric displacement vector and electric field vector respectively. $\mathbf{c}$, $\mathbf{e}$ and $\boldsymbol{\chi}$ are respectively the elasticity matrix, the piezoelectric matrix and the dielectric permittivity tensor. For a piezoelectric patch with thickness $h_p \le h_b$, a voltage V applied to the electrodes will produce an electric field V/h_p. The constitutive equation in one-dimensional can be written as

$$\sigma_{11}=E_p\varepsilon_{11}-e_{31}\frac{V}{h_p} \quad (25)$$

where σ_{11} and ε_{11} are longitudinal stress and strain, respectively. E_p denotes the Young's modulus of the piezoelectric patch.

3.1 Modeling of Sensor

As the electric displacement produced on the sensor surface is directly proportional to the stress acting on the sensor, then the electric displacement D_S is given as

$$D_S=d_{31}E_p\,\varepsilon_x=e_{31}\,\varepsilon_x \quad (26)$$

where d_{31} and e_{31} are the piezoelectric constant and piezoelectric stress/charge constant, respectively, ε_x is the strain produced, $\varepsilon_x=z_s(\partial^2 w/\partial x^2)$, where $z_s=h_s+h_b/2$ is the distance between neutral axis of the beam and sensor layer.

The sensor output voltage V^s is obtained as

$$V^s=G_C\int_A D_S dA=G_C d_{31}E_p z_s b_s\int_0^{l_s}\frac{\partial^2 w(x,t)}{\partial x^2}dx \quad (27)$$

where G_C is the gain of the signal conditioning device.

Rewrite it in incremental form:

$$V^s=V_a^s+\Delta V^s \quad (28)$$

where V_a^s is the sensor voltage at time t_a, ΔV^s is the sensor voltage increment in step time Δt, it is given by

$$\Delta V^s=-G_c e_{31}b_s z_s\int_0^{l_s}\frac{\partial^2\Delta w}{\partial x^2}dx \quad (29)$$

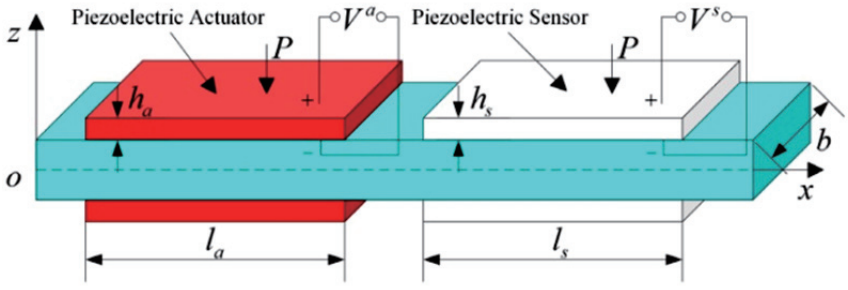


Fig. 8 Schematic of piezoelectric sensor and actuator.

https://doi.org/10.1017/jmech.2015.45 Published online by Cambridge University Press

when the increment of the angle displacement $\tilde{\theta}_1$ and $\tilde{\theta}_2$ is known, the increment of the deflection Δw can be drawn from Fig. 9.

$$\begin{aligned}\Delta w &= \frac{\Delta\hat{m}_{1z}(l_s-x)}{6l_sEI}(x^2-2l_sx)+\frac{\Delta\hat{m}_{1z}x}{6l_sEI}(l_s^2-x^2)\\ &=-\frac{(2\tilde{\theta}_1+\tilde{\theta}_2)(l_s-x)}{3l_s^2}(x^2-2l_sx)-\frac{(\tilde{\theta}_1+2\tilde{\theta}_2)x}{3l_s^2}(l_s^2-x^2)\\ &=\frac{x(l_s-x)(l_s\tilde{\theta}_1-x\tilde{\theta}_1-x\tilde{\theta}_2)}{l_s^2}\end{aligned} \tag{30}$$

Hence

$$\frac{\partial^2\Delta w}{\partial x^2}=\frac{-(4\tilde{\theta}_1+2\tilde{\theta}_2)l+6(\tilde{\theta}_1+\tilde{\theta}_2)x}{l^2} \tag{31}$$

Then

$$\Delta V^s=-G_ce_{31}b_sz_s(\tilde{\theta}_2-\tilde{\theta}_1) \tag{32}$$

3.2 Modeling of Actuator

When the actuator is driven by a control voltage V^a, the electric field on the actuator layer is $E_a=V^a/h_a$, then the strain produced by the electric field is given by

$$\varepsilon_a=d_{31}E_a \tag{33}$$

The stress σ_a produced by the actuator is given by

$$\sigma_a=E_p\,d_{31}\frac{V^a}{h_a} \tag{34}$$

This stress will produce a bending moment M_a act on the structure, it is given by

$$M_a=\int_0^{l_a}z\sigma_a dz=E_p\,d_{31}b_az_aV^a \tag{35}$$

where $z_a=h_a+h_b/2$ is the distance between neutral axis of the beam and actuator layer.

Then the control force vector acting on the element can be written as

$$\mathbf{f}^a=[0\ \ 0\ \ -M^a\ \ 0\ \ 0\ \ M^a]^T \tag{36}$$

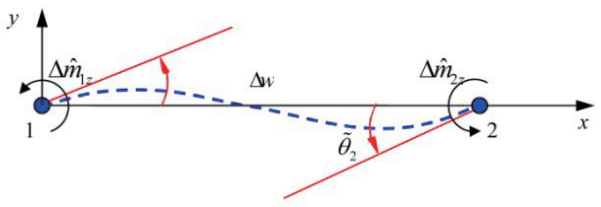


Fig. 9 The increment of the deflection.

Rewrite it in incremental form:

$$\mathbf{f}^a=\mathbf{f}_a^a+\Delta\mathbf{f}^a \tag{37}$$

where $\Delta\mathbf{f}^a=[0\ \ 0\ \ -\Delta M^a\ \ 0\ \ 0\ \ \Delta M^a]^T$ is the increment of the control force vector in step time Δt, and ΔM_a is given by

$$\Delta M_a=E_a\,d_{31}b_a\,z_a\,\Delta V^a \tag{38}$$

4. DESIGN OF DECENTRALIZED ADAPTIVE FUZZY CONTROLLER

4.1 Decentralized Strategy

As described before, the principal vibration modes of the membrane SAR antenna are the first order bending vibration mode and torsion vibration mode. In order to suppress these two kinds of vibration, two pairs of sensor and actuator are implemented. This control system is an MIMO system. It is hard to design an MIMO controller. Hence, the control system is decentralized into two control channels: Bending vibration control channel and torsion vibration control channel. For each channel, a MISO controller could be designed. The schematic diagram of the decentralized control system is shown Fig. 10.

In Fig. 10, S_1 and S_2 represent for the signal of the sensor 1 and sensor 2, respectively. S_b and S_t represent for the input signal bending and torsion vibration control channel, respectively. Their relationship is as follows:

$$\begin{cases}S_b=S_1+S_2\\ S_t=S_1-S_2\end{cases} \tag{39}$$

Similarly, C_1 and C_2 represent for the control signal of the actuator 1 and actuator 2, respectively. C_b and C_t represent for the control signal of bending and torsion vibration control channel, respectively. Their relationship is as follows:

$$\begin{cases}C_1=C_b+C_t\\ C_2=C_b-C_t\end{cases} \tag{40}$$

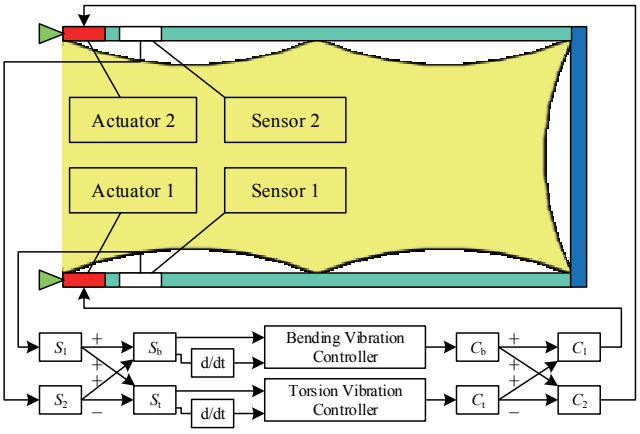


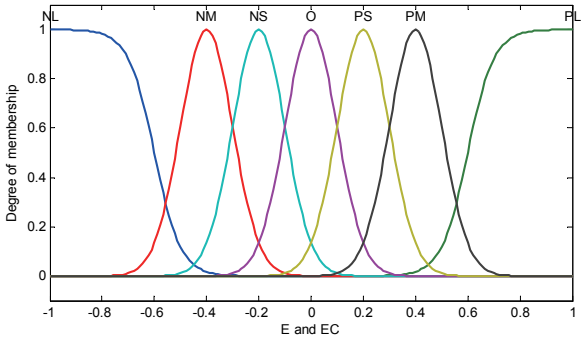
Fig. 10 Schematic diagram of the decentralized control system.

https://doi.org/10.1017/jmech.2015.45 Published online by Cambridge University Press

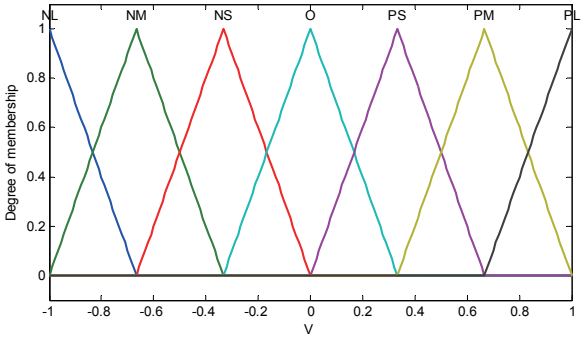
4.2 Design of Fuzzy Controller

As the system is decentralized into two control channels: Bending vibration control channel and torsion vibration control channel. Two same standard fuzzy controllers can be used for both channels. The controllers receive S_b and S_t as the error input, $\dot{S}_b$ and $\dot{S}_t$ as error change input, respectively, while gives the control voltage C_b and C_t as output, respectively. Fuzzy Toolbox of Matlab is used to construct the standard Mamdani fuzzy controllers. The MOM (mean of maximum) defuzzification method is used to create the defuzzified output value.

Seven fuzzy sets (NL, NM, NS, ZO, PS, PM, PL), two input power sets (E, EC), and one output power set (U) are used. The labels NL, NM, NS, ZO, PS, PM, PL refer to the linguistic values: Negative large, negative medium, negative small, zero, and positive small, positive medium and positive large, respectively. The sigmoidal membership functions and symmetric Gaussian membership functions are used for input power set, displayed in Eq. (41) and Fig. 11(a). The triangular membership functions are used for output power set, presented in Fig. 11(b).



(a) Membership function of input power set



(b) Membership function of output power set

Fig. 11 Membership function plots of the input and output power set.

$$\begin{cases} \mu_{F_i^1}(x_i) = \dfrac{1}{1+\exp\left(20(x_i+0.6)\right)} \\ \mu_{F_i^2}(x_i) = \exp\left(-50(x_i+0.4)^2\right) \\ \mu_{F_i^3}(x_i) = \exp\left(-50(x_i+0.2)^2\right) \\ \mu_{F_i^4}(x_i) = \exp(-50x_i^2) \\ \mu_{F_i^5}(x_i) = \exp\left(-50(x_i-0.2)^2\right) \\ \mu_{F_i^6}(x_i) = \exp\left(-50(x_i-0.4)^2\right) \\ \mu_{F_i^7}(x_i) = \dfrac{1}{1+\exp\left(-20(x_i-0.6)\right)} \end{cases} \tag{41}$$

For the MISO fuzzy control system, the lth AND- type rule is defined as follows:

Rule^l: IF x_1 is A_1^l and x_2 is A_2^l … and x_n is A_n^l THEN y is B^l (42)

where Rule^l denotes the lth fuzzy rule, $l = 1,2,\ldots,M$. M is the number of rules in rule base. x_i and y represent the input and output variables of the fuzzy logic system, $x_i \in [-E, E]$, $y \in [-U, U]$. A_i^l and B^l are the membership function of the input and output variables, respectively. Then fuzzy system can be represent as an n piecewise interpolation function:

$$f(x) = \frac{\sum_{l=1}^{M} \bar{y}^l \left(\prod_{i=1}^{n} \mu_{A_i^l}(x_i) \right)}{\sum_{l=1}^{M} \left(\prod_{i=1}^{n} \mu_{A_i^l}(x_i) \right)} \tag{43}$$

Let $\boldsymbol{\theta} = [\bar{y}_1, \cdots, \bar{y}_M]^T$ represent for consequent parameter vector, $\boldsymbol{\xi}(x) = [\xi_1(x), \cdots, \xi_M(x)]^T$, $\xi_l(x) = \prod_{i=1}^{n} \mu_{A_i^l}(x_i)$ represent for the fuzzy basis function. As $\sum_{l=1}^{M} \left(\prod_{i=1}^{n} \mu_{A_i^l}(x_i) \right) = 1$, the fuzzy system can be simplified as:

$$f(x) = \sum_{l=1}^{M} \theta_l \xi_l(x) = \boldsymbol{\theta}^T \boldsymbol{\xi}(x) \tag{44}$$

In this paper, 49 AND-type rules are used to describe the present fuzzy control system. All rules have weights equal to 1. These rules are presented in Table 1. The first row and the first column of this table are the inputs from the system and the others are the output of the fuzzy logic controller. The knowledge about the vibrating beam is employed in constructing this rule base. The fuzzy inference system output surface is shown in Fig. 12.

4.3 Adaptive Law

As the input and output universes of the classic fuzzy control method are fixed, it is hard to reach an accurate

https://doi.org/10.1017/jmech.2015.45 Published online by Cambridge University Press

stable control result. The variable universe adaptive fuzzy control method is implemented in this paper, the schematic diagram is shown in Fig. 13. Introduce $\alpha_i(x_i(k))$ and $\beta(y(k))$ as the contraction-expansion factors of the input and output universes, respectively. The fuzzy system can be represent as follows:

$$y(k+1)=\beta(y(k))\sum_{l}^{M}\bar{y}^{l}\left(\prod_{i=1}^{n}\mu_{A_i^l}\left(\frac{x_1(k)}{\alpha_1(x_1(k))}\right)\right) \tag{45}$$

Let $\xi(\alpha,x)=\left[\xi_1(\boldsymbol{\alpha},x),\xi_2(\boldsymbol{\alpha},x),\cdots,\xi_M(\boldsymbol{\alpha},x)\right]^T$ represent for the variable fuzzy basis function, where $\xi_l(\boldsymbol{\alpha},x)=\prod_{i=1,\cdots,n}\mu_{A_i^l}\left(\frac{x_i(k)}{\alpha_i(x_i(k))}\right)$, $l=1,2,\cdots,M$. Then the variable universe fuzzy system can be written as:

Table 1 Fuzzy IF-THEN rule base.

u \ $\dot{u}$	NL	NM	NS	ZO	PS	PM	PL
NL	NL	NL	NL	NM	ZO	ZO	ZO
NM	NL	NL	NL	NS	ZO	ZO	PS
NS	NL	NL	NM	ZO	ZO	PS	PM
ZO	NL	NM	NS	ZO	PS	PM	PL
PS	NM	NS	ZO	ZO	PM	PL	PL
PM	NS	ZO	ZO	PS	PL	PL	PL
PL	ZO	ZO	ZO	PM	PL	PL	PL

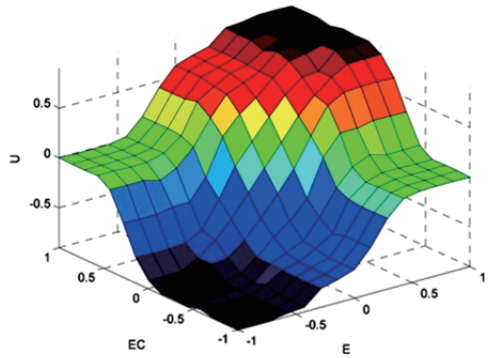


Fig. 12 Fuzzy inference system output surface.

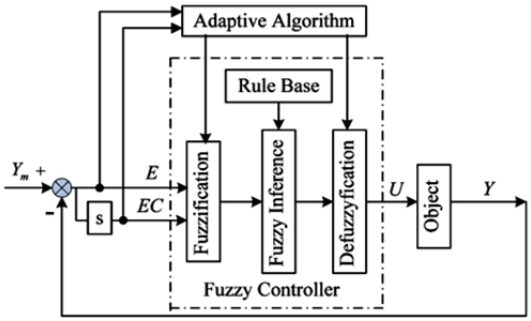


Fig. 13 Schematic diagram of the variable universe adaptive fuzzy controller.

$$f(\boldsymbol{\alpha},\beta,x)=\beta\boldsymbol{\theta}^T\boldsymbol{\xi}(\boldsymbol{\alpha},x) \tag{46}$$

Take the exponential-type contraction-expansion factor:

$$\alpha_i(x_i(k))=1-\lambda_i\exp\left(-k_i x_i(k)^2\right),\quad \lambda_i\in(0,1),k_i>0 \tag{47}$$

In this paper, α_1 and α_2 stands for the error factor and error change rate factor, respectively. If the error factor α_1 increases, the stiffness of the dynamic system increases. If the error change rate factor α_2 increases, the damping coefficient increases. However, if α_1 or α_2 is too small, the control system will be too sensitive and cause energy waste. Hence, threshold values are setting for α_1 and α_2. As the control voltage of the actuator is limited, that means the output universes is limited, hence we set $\beta(y(k))\triangleq\beta_0$ for simplicity.

5. NUMERICAL RESULTS AND DISCUSSIONS

5.1 Parameters

A membrane SAR antenna (half model) with the length 6 m and the width 3 m is considered here. The support frame is simplified as beams with cross section 5×10^{-3}m^2.The thickness of the membrane is 1mm. The elastic modulus of the support frame and the membrane are 7×10^{10} Pa and 3.5×10^{9} Pa, respectively. The frequency of the first bending and torsion mode are 0.32Hz and 1.59Hz, respectively. The equivalent piezoelectric constant is 5.6×10^{-8}m/V. The size of time step is 1×10^{-5}s. The damping coefficient is 0.005. The threshold value for the error factor and error change rate factor are set as 0.3 in AFC.

5.2 Shape Finding

Before the dynamic analysis of prestressed membranes, form finding analysis should be carried out first. The form finding analysis of membrane structures is to find the geometry shape and the corresponding stress distribution on the membrane surface. The final membrane shape is determined by the boundary conditions (support geometry, fixed or cable edges) and form finding properties (membrane and edge cable prestressed forces) [23].

The initial shape of the membrane SAR antenna is shown in Fig. 14(a). The membrane is meshed by 10×20 quadrangle elements. The tension cables are located on the edges of the membrane, and connected to the support frame on the six red points. The tension force in the cables is 8KN. When the initial stresses in the membrane are 1MPa, 2MPa and 3MPa, the equilibrium shape are shown in Figs. 14(b), 14(c) and 14(d), respectively. The results indicate that: The curvature of the tension cables is strongly enhanced with the stresses in the membrane.

5.3 Vibration Control

In this section, two kinds of vibration (bending and torsion vibration) and two kinds of disturbance (initial

https://doi.org/10.1017/jmech.2015.45 Published online by Cambridge University Press

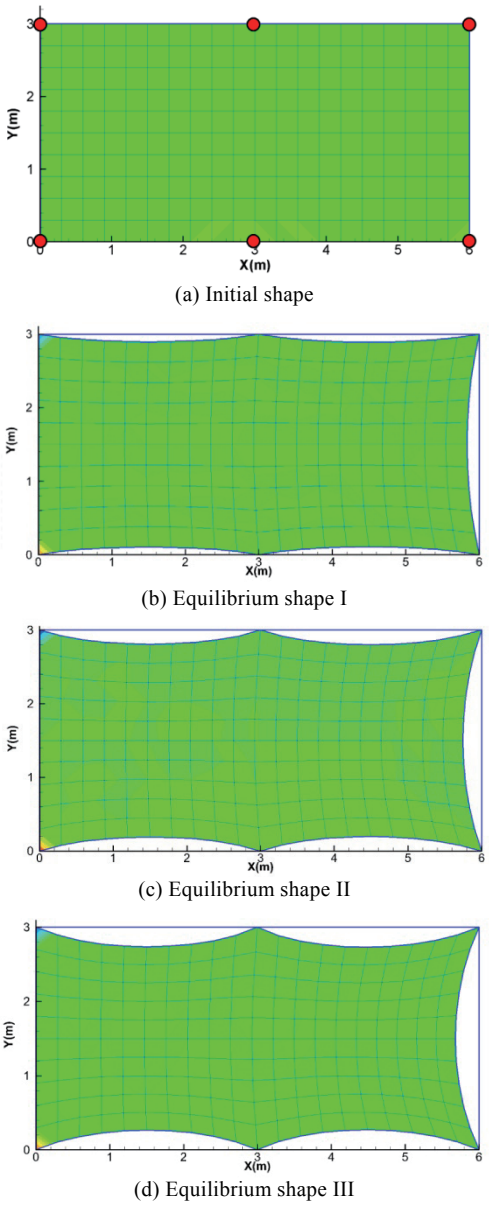
displacement disturbance and white noise disturbance) are considered. In order to compare the performance of different control method, the fuzzy controller (FC) and the adaptive fuzzy controller (AFC) are implemented in this paper.

5.3.1 Initial displacement disturbance response

In this simulation case, initial bending and torsion displacement disturbance fields are applied to the membrane structure, shown in Fig. 15. The closed-loop tip displacements and the torsion angel of the smart antenna with the FC and AFC are compared with the open-loop response in Figs. 16 and 18, respectively. It can be seen that both FC and AFC can suppress the vibration very efficiently. The control voltages of FC and AFC are plotted in Figs. 17 and 19, respectively, it can be seen that the peak values of the control voltage not exceed the allowable range. Another important phenomenon should be noticed that: The control effect of FC and AFC are almost the same at the first 30s and 10s of the bending vibration case and torsion vibration case, but after that time, AFC presents an much better performance than FC. It is because the adaptive law can scale the input universes when the vibration amplitude is small.

5.3.2 White noise disturbance response

In this simulation case, a centralized Gaussian white noise load is applied on the tip corner of the antenna. The open-loop and closed-loop tip displacements and control voltages with FC and AFC are present in Figs. 20 and 21. The standard deviation of open-loop, FC and AFC are 0.0310m, 0.0121m and 0.0102m, respectively. It demonstrates that both FC and AFC manage to reduce the vibration significantly.



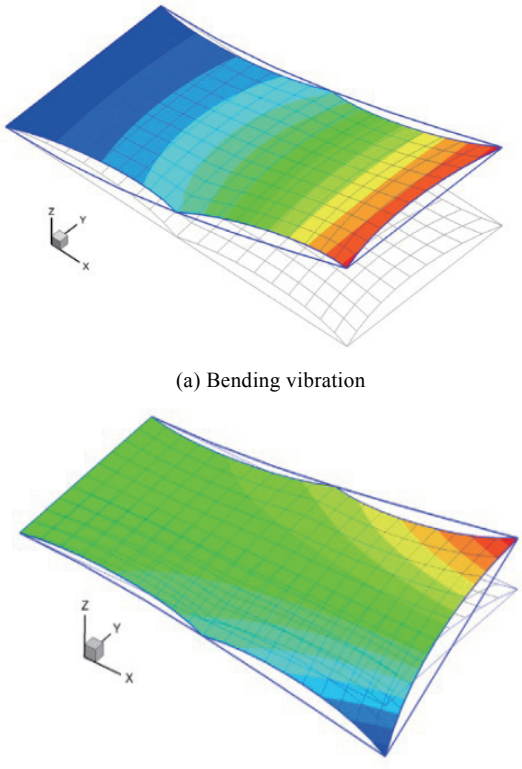
(a) Initial shape

(b) Equilibrium shape I

(c) Equilibrium shape II

(d) Equilibrium shape III

Fig. 14 Shape finding of the membrane SAR antenna.



(a) Bending vibration

(b) Torsion vibration

Fig. 15 Vibration of the membrane SAR antenna.

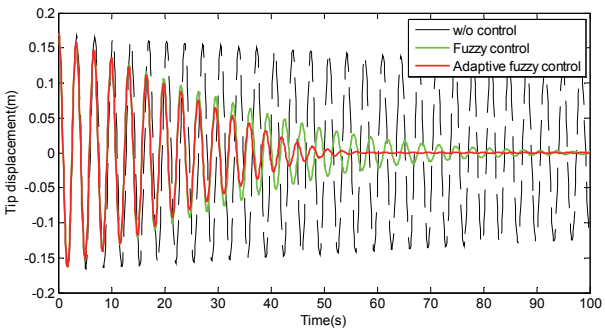


Fig. 16 Tip displacement for an initial bending displacement field.

https://doi.org/10.1017/jmech.2015.45 Published online by Cambridge University Press

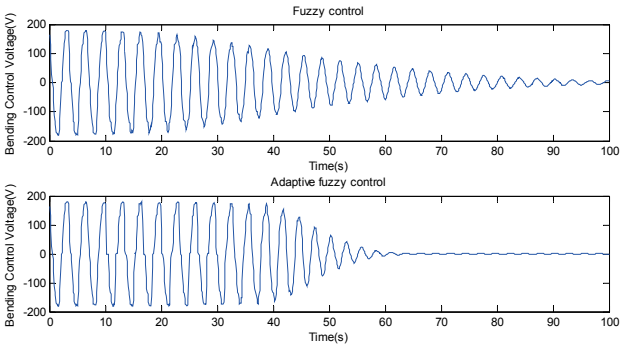


Fig. 17 Control voltage for an initial bending displacement field.

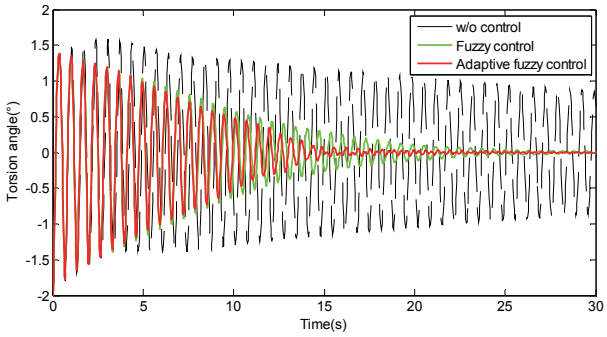


Fig. 18 Torsion angle for an initial torsion displacement field.

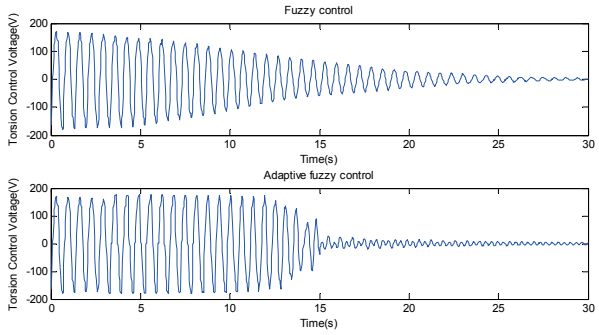


Fig. 19 Control voltage for an initial torsion displacement field.

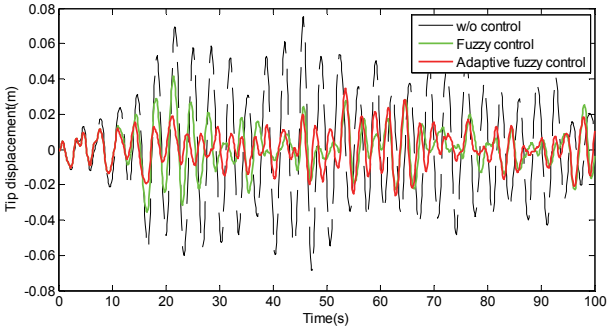


Fig. 20 Tip displacements for white noise disturbance.

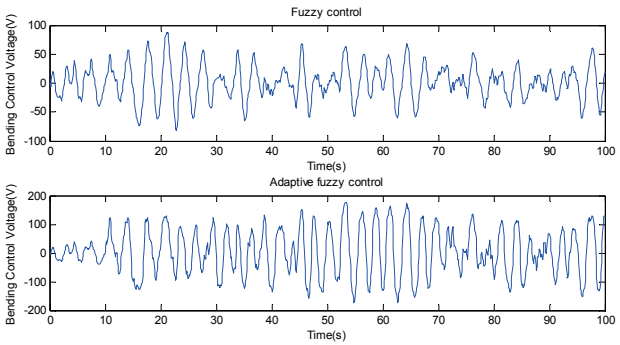


Fig. 21 Control voltage for white noise disturbance.

6. CONCLUSIONS

This article addressed the vibration control problem of membrane SAR antenna structure. The VFIFE method is used to build up the model of the membrane SAR antenna structure with piezoelectric sensors and actuators. The four nodes membrane element, sensor element and actuator element for VFIFE are presented. Decentralized adaptive fuzzy vibration controller is designed. In the numerical experiment part, form finding is first carried out, then vibration control simulations are studied. According to the presented study, the following conclusions can be drawn:

1 For structure composed of beam, cable and membrane, VFIFE method can do shape finding analysis, static analysis and dynamic analysis in one model. It means this method can reduce the work amount and minimize data exchange.

2. The application of VFIFE method can be extended to the control of smart structure. It is very appropriate to linked with model-free control method, such as fuzzy control method.

3. The large amplitude vibration of large flexible structures can be suppressed to small amplitude vibration quickly. However, the small amplitude vibration will last for a long time with fuzzy control due to the small control input. Adaptive fuzzy controller can adaptively scale the control input, then it can obtain a better control performance due to suppressing small amplitude vibration.

ACKNOWLEDGEMENTS

R. Xu wishes to thank Dr. Y.H. Liao of National University of Defense Technology for all his kindness and help. This work was supported by the "Twelfth Five" National Defense Preresearch Program Foundation of China.

REFERENCES

1. Huang, J., Lou, M. and Caro, E., "Super-Low-Mass Spaceborne SAR Array Concepts," *Antennas and*

https://doi.org/10.1017/jmech.2015.45 Published online by Cambridge University Press

Propagation Society International Symposium, Montreal, Quebec, Canada (1997).
2. Leipold, M., Runge, H. and Sickinger, C. "Large SAR Membrane Antennas with Lightweight De-ployable Booms," *28th ESA Antenna Workshop on Space Antenna Systems and Technologies*, ESA/ESTEC, Noordwijk,Netherlands (2005).
3. Amezquita-Sanchez, J. P., *et al*., "Vibration Control on Smart Civil Structures: A Review," *Mechanics of Advanced Materials and Structures*, **21**, pp. 23–38 (2013).
4. Li, D.-X., Liu, W. and Jiang, J.-P., "Optimal Place-ment of Controls for Truss Structures in Space," *IEEE Intelligent Systems*, **27**, pp. 51–56 (2012).
5. Li, D.-X. and Xu, R., "Optimal Design and Control of Smart Space Structures: A Memetic Evolution Approach," *Intelligent Systems, IEEE*, **29**, pp. 40–46 (2014).
6. Li, D. and Xu, R., "Autonomous Decentralized Intel-Ligent Vibration Control for Large Split-Blanket Solar Arrays," *Science China-Technological Sciences*, **56**, pp. 703–712 (2013).
7. Qiu, Z.-C., *et al*., "Vibration Control of Two-Connected Piezoelectric Flexible Plate Using Nonlinear Algorithm and T-S Fuzzy Controller," *Journal of Intelligent Material Systems and Structures*, **26**, pp. 1–25 (2014).
8. Sales, T. P., Rade, D. A. and De Souza, L. C. G., "Pas-Sive Vibration Control of Flexible Spacecraft Using Shunted Piezoelectric Transducers," *Aerospace Science and Technology*, **29**, pp. 403–412 (2013).
9. Li, W. P. and Huang, H., "Integrated Optimization of Actuator Placement and Vibration Control for Piezoelectric Adaptive Trusses," *Journal of Sound and Vibratio*n, **332**, pp. 17–32 (2013).
10. Ting, E. C., Shih, C. and Wang, Y. K., "Fundamentals of a Vector form Intrinsic Finite Element: Part II. Plane Solid Elements," *Journal of Mechanics*, **20**, pp. 123–132 (2004).
11. Ting, E. C., Shih, C. and Wang, Y. K., "Fundamentals of a Vector form Intrinsic Finite Element: Part I. Basic Procedure and a Plane Frame Element," *Journal of Mechanics*, **20**, pp. 113–122 (2004).
12. Shih, C., Wang, Y. K. and Ting, E. C., "Fundamentals of a Vector form Intrinsic Finite Element: Part III. Convected Material Frame and Examples," *Journal of Mechanics*, **20**, pp. 133–143 (2004).
13. Wang, C. Y., *et al.*, "Nonlinear Dynamic Analysis of Reticulated Space Truss Structures," *Journal of Mechanics*, **22**, pp. 199–212 (2006).
14. Wang, C.-Y., Wang, R.-Z. and Tsai, K.-C., "Numerical Simulation of the Progressive Failure and Collapse of Structure Under Seismic and Impact Loading," *4th International Conference on Earthquake Engineering*, Taipei, Taiwan (2006).
15. Wu, T. Y., Wang, R. Z. and Wang, C. Y., "Large De-Flection Analysis of Flexible Planar Frames," *Journal of the Chinese Institute of Engineers*, **29**, pp. 593–606 (2006).
16. Wu, T.-Y., Tsai, W.-C. and Lee, J.-J., "Dynamic Elastic—Plastic and Large Deflection Analyses of Frame Structures Using Motion Analysis of Structures," *Thin-Walled Structures*, **47**, pp. 1177–1190 (2009).
17. Wu, T. Y., *et al*., "Motion Analysis of 3D Membrane Structures by a Vector form Intrinsic Finite Element," *Journal of the Chinese Institute of Engineers*, **30**, pp. 961–976 (2007).
18. Wu, T. Y. and Ting, E. C., "Large Deflection Analysis of 3D Membrane Structures by a 4-Node Quadrilateral Intrinsic Element," *Thin-Walled Structures*, **46**, pp. 261–275 (2008).
19. Lien, K. H., *et al*., "Nonlinear Behavior of Steel Structures Considering the Cooling Phase of a Fire," *Journal of Constructional Steel Research*, **65**, pp. 1776–1786 (2009).
20. Lien, K. H., *et al*., "Vector form Intrinsic Finite Ele-Ment Analysis of Nonlinear Behavior of Steel Struc-Tures Exposed to Fire," *Engineering Structures*, **32**, pp. 80–92 (2010).
21. Lien, K. H., Chiou, Y. J. and Hsiao, P. A., "Vector form Intrinsic Finite-Element Analysis of Steel Frames with Semirigid Joints," *Journal of Structural Engineering*, **138**, pp. 327–336 (2012).
22. Wu, T.-Y., "Dynamic Nonlinear Analysis of Shell Structures Using a Vector form Intrinsic Finite Ele-Ment," *Engineering Structures*, **56**, pp. 2028–2040 (2013).
23. Gosling, P. D., *et al*., "Analysis and Design of Mem-Brane Structures: Results of a Round Robin Exercise," *Engineering Structures*, **48**, pp. 313–328 (2013).

(Manuscript received October 15, 2014,
accepted for publication January 30, 2015.)

https://doi.org/10.1017/jmech.2015.45 Published online by Cambridge University Press